

An Analysis of LIGO Glitches Using t-SNE During the First Part of the Fourth LIGO-Virgo-KAGRA Observing Run

Tabata Aira Ferreira, Gabriela González, Osvaldo Salas

Louisiana State University, Baton Rouge, LA 70803, USA

E-mail: tferreira@lsu.edu

Abstract. This paper presents an analysis of noise transients observed in LIGO data during the first part of the fourth observing run, using the unsupervised machine learning technique t-distributed Stochastic Neighbor Embedding (t-SNE) to examine the behavior of glitch groups. Based on the t-SNE output, we apply Agglomerative Clustering in combination with the Silhouette Score to determine the optimal number of groups. We then track these groups over time and investigate correlations between their occurrence and environmental or instrumental conditions. At the Livingston observatory, the most common glitches during O4a were seasonal and associated with ground motion, whereas at Hanford, the most prevalent glitches were related to instrumental conditions.

1. Introduction

Gravitational waves, predicted by Einstein’s general theory of relativity, have revolutionized our understanding of astrophysical phenomena by providing a new observational window into the Universe. Since the first direct detection of gravitational waves in 2015 by the Laser Interferometer Gravitational-Wave Observatory (LIGO) and the Virgo collaboration [1], ground-based detectors have been actively searching for signals during dedicated observing runs. Together with Virgo in Italy [2] and KAGRA in Japan [3], LIGO forms the LVK collaboration, which brings together a large community of researchers working toward the common goal of detecting an increasing number of gravitational-wave events.

LIGO consists of two observatories designed to detect these spacetime ripples: one located in Hanford, Washington (LHO), and the other in Livingston, Louisiana (LLO). During gravitational wave searches, observatories operate in observing mode, and between observing runs, planned pauses are implemented to upgrade instrumentation and improve sensitivity [4]. The first detection occurred during the first observing run (O1), which lasted from September 12, 2015, to January 2016. On January 16, 2024, LIGO concluded the first part of its fourth observing run (O4a), which had started on May 24, 2023. As registered in the Gravitational-Wave Candidate Event Database

(GraceDB) [5], there are already more than two hundred significant detection candidates identified during O4 produced by the mergers of compact objects such as black holes and neutron stars.

LIGO also records various noise transients arising from instrumental or environmental factors, including ground motion, wind, and other disturbances [6, 7]. These non-astrophysical transient signals are commonly referred to as *glitches*. Glitches are non-stationary artifacts that contribute to the background in gravitational wave searches [8–10] and, in some cases, can closely mimic signals from compact binary coalescences (CBC). Efforts within CBC searches to mitigate this challenge are therefore essential and rely on different pipelines, such as PyCBC [11, 12], GstLAL [13, 14], MBTA [15, 16], and SPIIR [17–19], which incorporate likelihood weighting and other strategies to reduce the impact of glitches on search sensitivity.

Glitch morphologies are typically analyzed using spectrograms [20], which facilitate their classification into distinct glitch groups. Different tools have been developed to analyze these unwanted signals. BayesWave [21, 22] and AWaRe [23], for instance, employ distinct approaches to reconstruct gravitational-wave signals contaminated by glitches. *gengli* [24, 25] is an open-source glitch generator useful to support a variety of testing and validation tasks, while other tools focus on glitch classification, improving classifier performance, or distinguishing true astrophysical signals from spurious noise transients [26–30]. One example is Gravity Spy, an interdisciplinary project that integrates machine learning, citizen science, and input from LIGO scientists to classify glitches [31, 32]. Glitches are named based on their morphology and/or known or suspected physical origin. Examples of their spectrogram morphologies can be found in [8, 32–34].

The main motivation behind these efforts is to support the overarching goal of glitch studies: identifying their physical origin to eliminate or mitigate their impact on gravitational-wave detection. This work presents an analysis of the main glitch groups observed during O4a, investigating their potential correlations with environmental and/or instrumental variations using the methodology detailed in [35]. This investigation identifies patterns among glitches using the information provided by *Omicron* [36, 37], the primary tool in LIGO used to detect noise transients in detector data. When excess power is identified in the data, *Omicron* characterizes it by analyzing its time-frequency tiles in spectrograms produced from the *Q*-transform [38]. This information is stored in unclustered files, and after preparing these data, we employ t-distributed Stochastic Neighbor Embedding (t-SNE) [39], a dimensionality reduction technique, to project the high-dimensional output of *Omicron* (which includes numerous tile-based features) into a two-dimensional space.

As an unsupervised technique, t-SNE does not require prior knowledge or a training dataset. Instead, it relies on probability-based similarity between data points to preserve local relative distances in the lower-dimensional representation. This makes t-SNE particularly useful for uncovering patterns in data without predefined assumptions. The resulting projections often reveal meaningful structures; as shown in [35, 40], cross-

checking the clusters obtained from t-SNE with Gravity Spy labels demonstrates that, when applied to unclustered Omicron information, t-SNE produces groups that closely correspond to known glitch classes.

In this work, the primary objective is to track the temporal evolution of glitches during the O4a observing run. To facilitate this analysis, we first apply t-SNE to project the high-dimensional data into a two-dimensional space and then use *Agglomerative Clustering* [41] to group similar glitches and assign labels. The *Silhouette Score* [42] is used to evaluate clustering quality and determine the optimal number of groups. These group labels serve primarily as a means to organize and visualize the temporal behavior of distinct glitch populations, to support their possible association with environmental or instrumental conditions, and to enable the classification of previously unseen data. This approach is entirely unsupervised and based solely on features derived from Omicron triggers. Further details about the method can be found in [35].

The paper is structured as follows. Section 2 presents the glitch population observed at LLO during O4a, together with an analysis of ground motion across different frequency bands. The section also evaluates the correlation between ground motion and glitch rate, highlighting how the low-frequency glitches impacted the interferometer during the analyzed observing period. A parallel analysis for LHO is provided in Section 3, focusing on the evolution of broadband glitches during O4a, which were primarily associated with internal instrumentation couplings rather than environmental factors. Finally, Section 4 summarizes and discusses the key findings of this work.

2. Glitches during O4a at LLO

The rate of glitches with a signal-to-noise ratio (SNR) exceeding 10 at LLO was higher during O4a (approximately 31 glitches per hour) compared to the third observing run, O3 (approximately 26 glitches per hour) [7]. The glitch rate during O3 was significantly influenced by the prevalence of scattering glitches, which dominated the transient population in that period. Scattering glitches occur when stray light couples back into the main beam after interacting with surfaces, whose identification is particularly challenging. Substantial efforts during O3 successfully identified and mitigated some of these scattering surfaces, resulting in a considerable reduction in the occurrence of such glitches [43, 44].

Despite these mitigation efforts, the transient rate during O4a surpassed that of O3; this increase was primarily driven by glitches occurring at low frequencies. Figure 1 illustrates the distribution of glitch frequencies below 100 Hz at LLO during O4a, highlighting this trend. The apparent gap in glitches around 14 Hz is due to masking by noise from the test masses’ roll modes and calibration lines at those frequencies. Additional peaks are also visible in the histogram, notably around 32, 39, 49, 61, 75, and 93 Hz. We compare the GravitySpy classes [32] in each of these frequency bins, and spectrogram analysis shows that the *Tomte* class accounts for more than 50% of glitches with peak frequencies near 32 and 39 Hz, while the 49 Hz peak consists of approximately

50% *Blip Low Frequency*. At 61 Hz, the dominant class is *Blip Low Frequency*; the peak around 75 Hz is primarily associated with *Koi Fish*, and the 93 Hz region includes a mix of *Koi Fish* and other classes. Some classes can share similar peak frequencies, but due to the complex nature of glitches, peak frequency alone is usually insufficient to distinguish between certain groups. This underscores the importance of analyzing glitches based on their morphology.

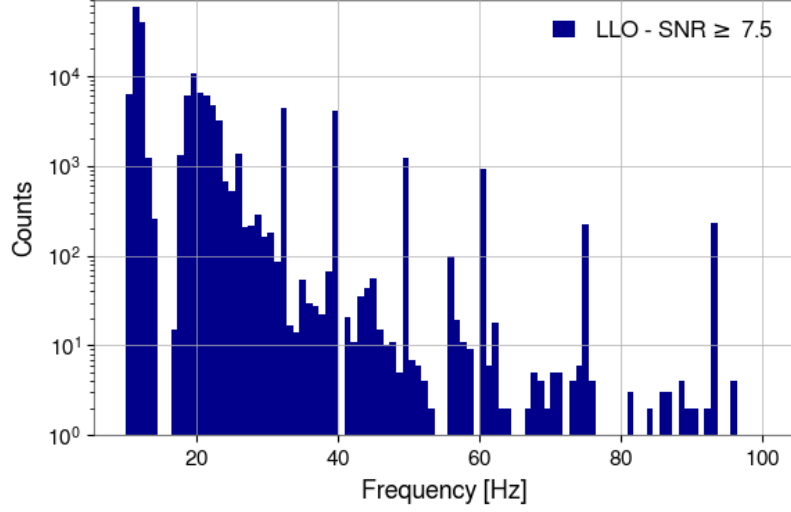


Figure 1: Histogram of frequencies of glitches during O4a, with $\text{SNR} \geq 7.5$. This shows the range where we observed the most common glitches at LLO during O4a, which occurred between 10 and 100 Hz.

The increase in glitch occurrence at lower frequencies is associated with the improved sensitivity of the interferometer in this frequency range [7]. Figure 2 illustrates this by comparing the characteristic strain at low frequencies (10–30 Hz) during O3, shown in blue, with that of O4a, shown in pink. This comparison highlights the enhanced sensitivity of the interferometer during O4a, which resulted in a higher detection rate of glitches (and of gravitational waves) within this frequency range. The blue dots represent the amplitude of scattering glitches over an eight-hour period on December 27, 2019 (during O3). Since these glitches were associated with relatively high ground motion, we selected a day during O4a with similar ground motion amplitude, and also plotted the corresponding glitches, represented by pink squares. There are fewer glitches in O4 between 18 Hz and 30 Hz due to the scattering mitigation [43], but there is a higher rate in O4 at lower frequencies. While some high-amplitude glitches between 10 and 13 Hz were detectable during O3, most of the lower-frequency glitches observed during O4a would not have been “visible” during O3, given the sensitivity limitations of the interferometer at that time.

Figure 3 presents the average number of glitches per hour for each month during O4a, represented by the dark blue bars, considering glitches in the 10 to 2048 Hz range with a minimum SNR of 7.5. The glitch rate exhibited a general increase over time,

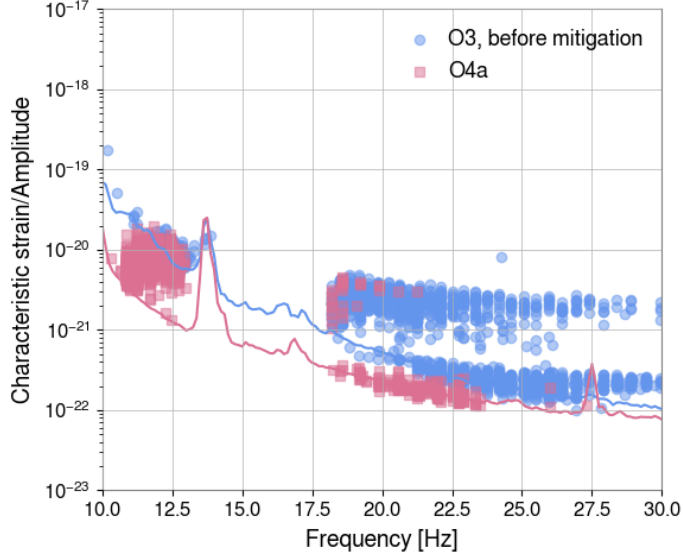


Figure 2: Characteristic strains during O3 in blue and O4a in pink, measured under similar microseismic motion amplitudes (or velocities). The blue circles highlight the impact of scattering glitches on the 18–30 Hz frequency band during O3, which was significantly reduced [43] in O4a (pink squares).

primarily driven by the low-frequency (below 25 Hz) glitch rate, represented by the light blue bars with diagonal hatching.

As mentioned earlier, high ground motion (or elevated ground velocities) was the primary cause of scattering transients during O3. One class of these transients, referred to as *Scattered Light* or *slow scattering* [43, 45], was characterized by arch-like features in their spectrograms. Given this, and based on the seasonal pattern in which ground motion in specific frequency bands tends to exhibit higher amplitudes during the winter months, we identified a potential correlation between such low-frequency glitches observed during O4a and elevated ground motion levels [46]. This behavior is further supported by the ground motion data shown later in Figure 11.

Ground motion at LIGO is measured by seismometers positioned at various locations around the interferometer, which record ground velocity, typically expressed in nanometers per second (nm/s). Measurements are taken along three axes: \hat{x} , aligned with the input laser, \hat{y} , perpendicular to \hat{x} ; and \hat{z} , representing vertical motion orthogonal to the x–y plane.

We analyze the Root Mean Square (RMS) of the ground motion within specific frequency ranges, known as Band-Limited RMS (BLRMS) [47]. The frequency bands considered correspond to the microseismic band—usually associated with ocean waves—and the anthropogenic band, which is generally linked to human activities such as passing trains or nearby vehicular traffic. The microseismic band is further subdivided into two distinct sub-bands. In this context, the analysis focuses on the following:

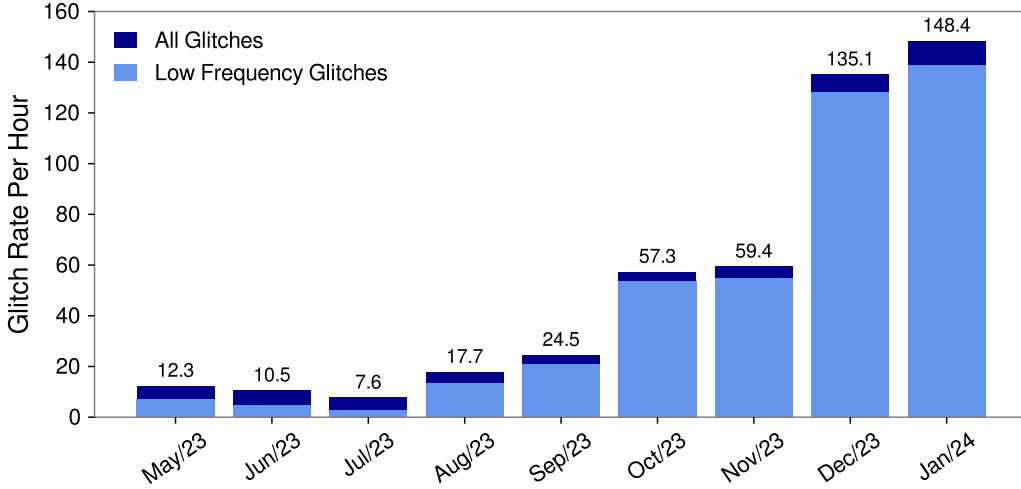


Figure 3: Average hourly glitch rates for each month during O4a. Dark blue bars, annotated with numerical values, represent the total rate of clustered Omicron transients with frequencies between 10 and 2048 Hz and a minimum SNR of 7.5. Light blue bars with hatching indicate the subset of glitches with frequencies below 25 Hz.

- **Lower MicroSeismic (LMS) band:** ground motion between 0.1 and 0.3 Hz, measured in the \hat{x} direction by the ETMY seismometer.
- **Higher MicroSeismic (HMS) band:** ground motion between 0.3 and 1 Hz, also measured in the \hat{x} direction by the ETMY seismometer..
- **Anthropogenic band:** ground motion between 1 and 3 Hz, measured in the \hat{z} direction by the ETMY seismometer.

As proposed in [35], we started selecting a dataset containing 1,500 randomly sampled glitches for each month during O4a (from May 2023 to January 2024). Since each month contains a different number of glitches, not applying a monthly filter would result in overrepresentation of glitches from months with higher glitch rates, which differ substantially from others, as shown in Figure 3. Starting from the unclustered Omicron triggers (panel 4a), each glitch was mapped onto a 30×41 time–frequency–Q matrix in which each bin stores the maximum normalized SNR of the triggers assigned to that bin (panel 4b). This matrix was then flattened into a 1,230-dimensional feature vector (panel 4c). The final dataset, therefore, contains 1,500 glitches per month over 9 months, totaling 13,500 samples, each described by 1,230 features. To prevent glitches with very high SNR from dominating the t-SNE output, we applied min-max normalization to the SNR components of each vector.

The t-SNE algorithm reduced the original 1,230-dimensional vector representation to two dimensions, enabling the visualization of 13,500 glitches on a 2D plane. This representation is shown in Figure 5a as a scatter plot of the two t-SNE output coordinates, where each point corresponds to a single glitch. Three major groups are

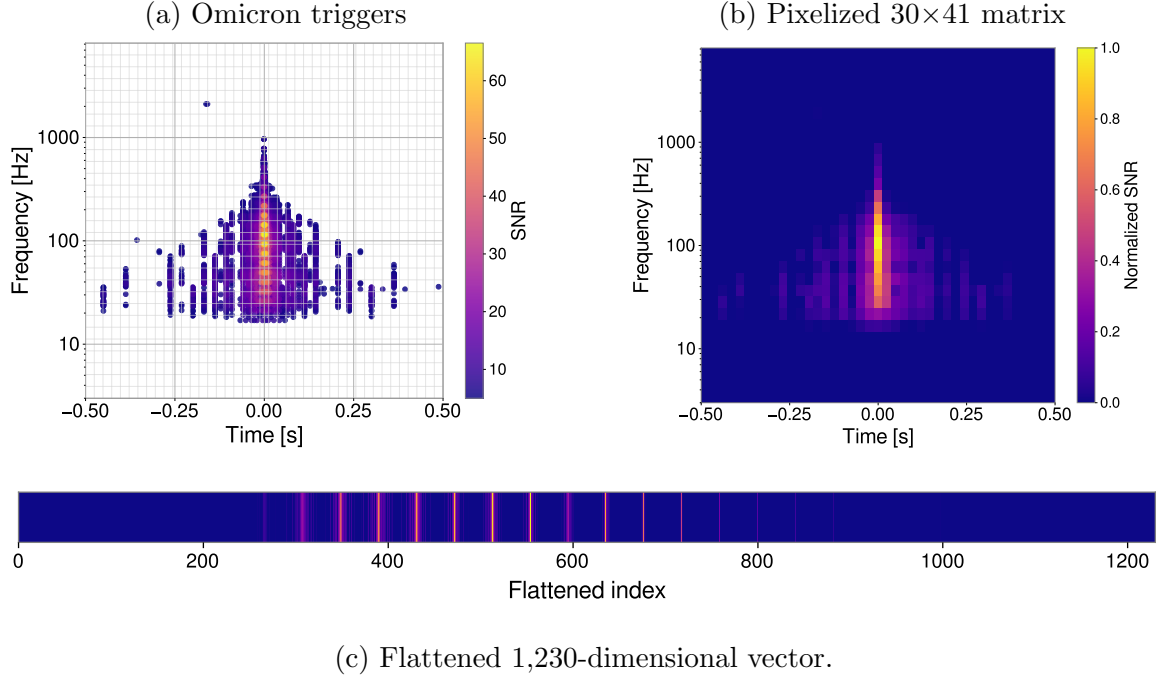


Figure 4: Workflow for constructing the vectors used as input to t-SNE, illustrated for one example glitch. (a) Omicron triggers in a ± 0.5 s window with the 30×41 time-frequency grid. (b) Pixelized glitchgram matrix with normalized SNR. (c) Flattened 1,230-dimensional vector, shown using the same colormap scale as in panel (b), used as input to t-SNE and clustering.

identifiable: the largest cluster is positioned on the left, the second cluster is located at the top right, and the third cluster appears at the bottom right.

Figure 5b presents the clusters identified via *Agglomerative Clustering*, using the optimal configuration determined by the *Silhouette Score*. Both techniques were implemented with the *Scikit-learn* library [48]. As expected, the clustering process revealed three main groups, referred to here as *Group L_1* (purple), *Group L_2* (green), and *Group L_3* (orange).

An important advantage of this method is its ability to analyze the temporal evolution of glitches. Figure 6 presents the t-SNE output filtered month by month during O4a, providing an overview of which group was more prominent in each month. As mentioned, we selected the same number of glitches per month, enabling a balanced temporal analysis and preventing the dominance of months with higher glitch rates. Although this approach introduces an artificial uniformity across months, it allows for a clearer comparison of cluster behavior over time at this scale. If we had instead selected a total of 13,500 glitches randomly, without monthly filtering, months with higher glitch rates (see Figure 3) would have dominated the sample. A more detailed discussion of this selection strategy is provided in [35].

The numbers displayed below each scatter plot represent the percentage

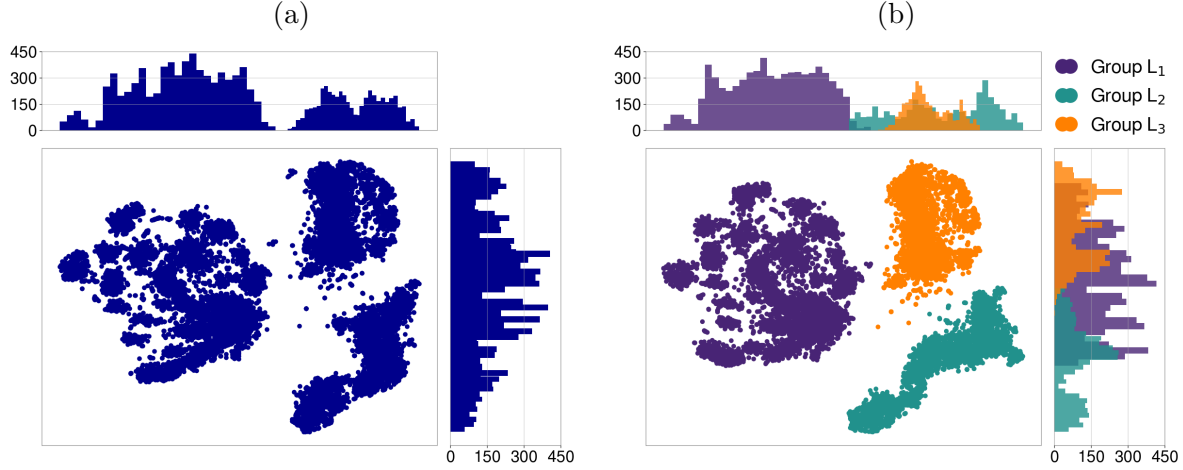


Figure 5: (a) Scatter plot of the 2D t-SNE output coordinates representing 13,500 data points, each originally embedded in a 1,230-dimensional space derived from unclustered Omicron triggers. Each point corresponds to a glitch. Histograms along the top and right axes illustrate the distribution of glitches along each coordinate. (b) The same t-SNE output, with points colored according to the classes assigned by *Agglomerative Clustering*.

contribution of each group for the respective month. Comparing May, June, and July reveals a high similarity in cluster distribution, with Group L_2 (green) being the most prominent during all three months. The gray contours behind the data points indicate the estimated density, computed using Kernel Density Estimation (KDE) as implemented in Seaborn [49], where darker regions correspond to areas with higher data point concentrations.

In August, Group L_1 begins to exhibit higher densities, accounting for more than 50% of the data. It slightly contracts in September (when an increase in the glitch rate from Group L_3 is observed) but remains the dominant group in subsequent months, reaching nearly 80% of the data in November. Group L_3 fluctuates over time but remains consistently present, with its highest predominance occurring in September. Conversely, from August onward, Group L_2 declines due to the increasing prominence of other clusters. In December, for instance, the low density of points in this region results in an almost complete absence of KDE contours. This does not imply the disappearance of Group L_2 , but rather that it was no longer among the most significant groups.

By examining the spectrograms, we observe that Group L_1 is dominated by glitches with arch-like structures at a frequency of approximately 12 Hz; examples are shown in Figure 7. Some of these glitches exhibit longer durations, others show repetitions over time, and some vary in the number of harmonics. Despite occurring at similar frequencies, these morphological differences explain the formation of mini-clusters within the group (see Figure 5). Glitches with similar morphological features

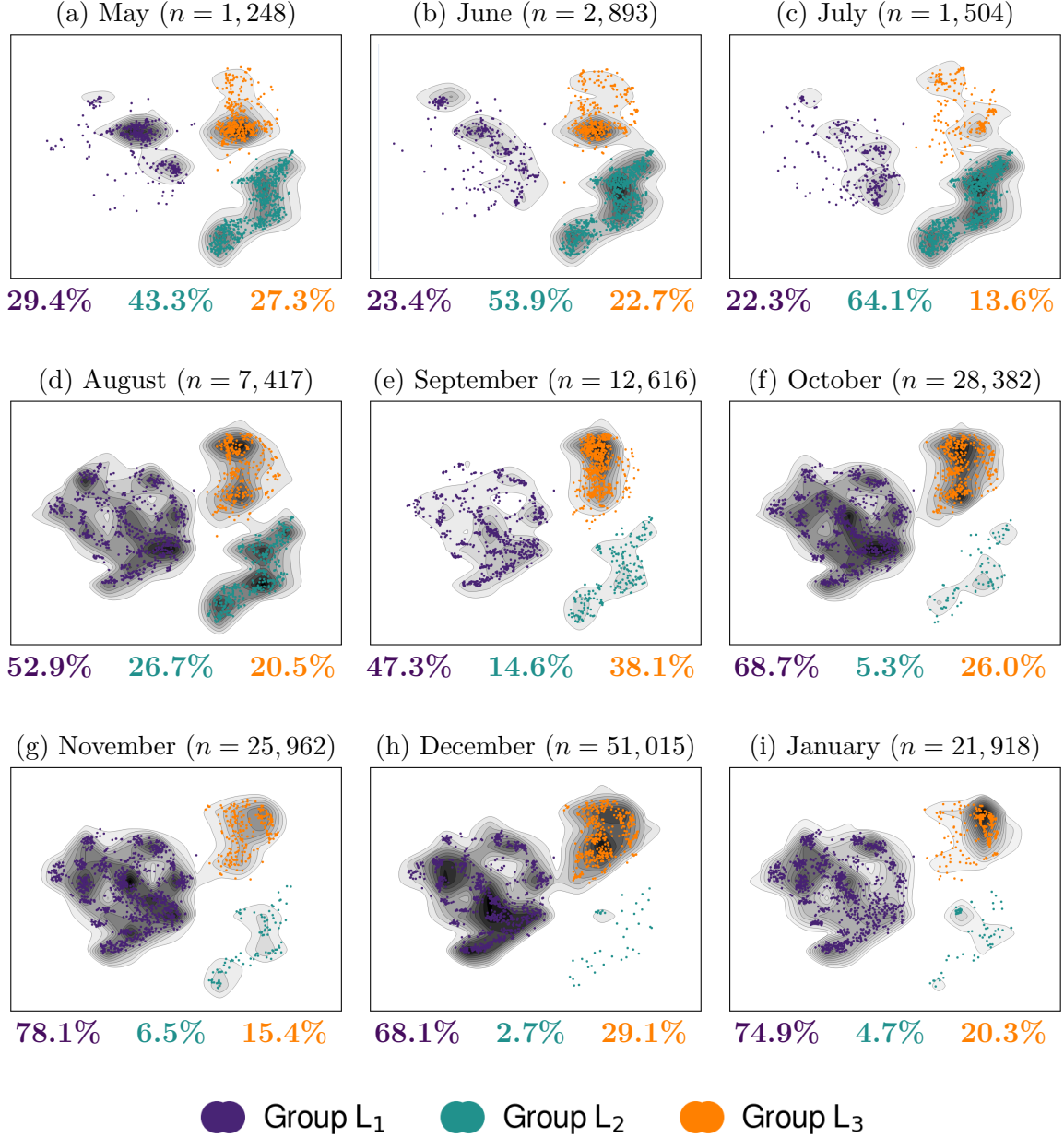


Figure 6: A scatter plot of the same t-SNE coordinates from LLO, filtered by month for each identified class. Each panel illustrates the behavior of the clusters during O4a, from May 2023 to January 2024. The value of n indicates the total number of glitches in that month, and the percentages represent the relative fraction of glitches assigned to each group based on the t-SNE output.

(arch-like patterns) are observed in Group L₃, but with a primary frequency around 20 Hz; examples of their spectrograms are presented in Figure 8.

Group L₂ primarily consists of glitch classes identified by Gravity Spy [50] as *Extremely Loud*, *Blip*, *Koi Fish*, *Tomte*, and others (examples are given in Figure 9). These glitches do not have a significant seasonal pattern (at least not as prominently as

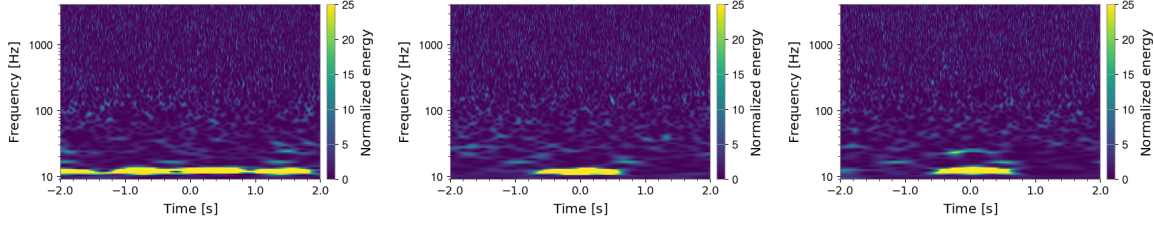


Figure 7: Examples of spectrograms present in Group L_1 . The spectrograms exhibit frequencies around 12 Hz, with variations in morphology.

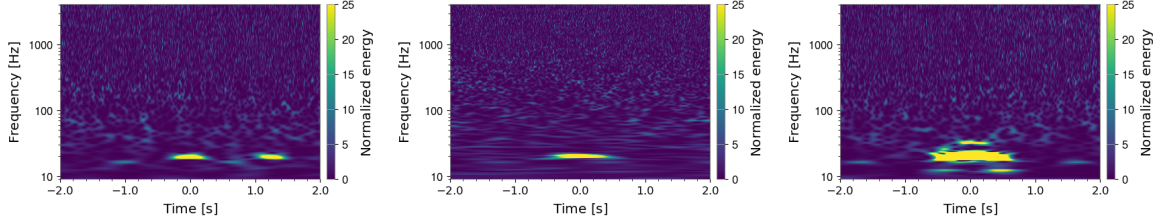


Figure 8: Examples of spectrograms present in Group L_3 . The spectrograms exhibit frequencies around 20 Hz, with variations in morphology.

those in Group L_1 and Group L_3), which results in Group L_2 gradually losing structure in the t-SNE output over time and being more dominant at the beginning of O4a, when the other groups were still less prominent. To further subdivide Group L_2 into its specific subclasses, it would be necessary to rerun t-SNE on this subset. However, as previously mentioned, the primary objective of this study is to understand the behavior of the most frequent glitches that most affected the detector during O4a and to investigate potential correlations with environmental sensors surrounding the interferometer.

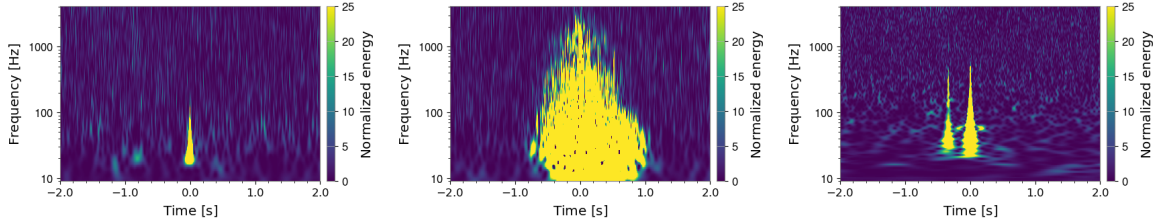


Figure 9: Examples of spectrograms present in Group L_2 .

Given the previous insights from the t-SNE output, we investigate possible relationships between the identified groups and seismic noise. In general, amplitude variations in ground motion across the three directions exhibit similar overall trends. [Appendix A](#) presents a study of seismometers installed at different locations, illustrating this behavior and providing pairwise comparisons between them. The ETMY location exhibits a higher amplitude in the anthropogenic band, which led to its seismometer being chosen as the reference in this analysis — although any of the seismometers could have been selected.

Figure 10 shows the ground motion measured by the seismometer at ETMY (in the \hat{z} direction) within the anthropogenic band, which does not present a clear correlation with the glitches identified in the t-SNE output. The figure displays the daily median motion in the anthropogenic band for June, October, and December, with the corresponding first and third quartiles indicated by the shaded regions. The remaining months follow a similar pattern, characterized by increased motion on weekdays—primarily due to nearby traffic—and significantly reduced motion on weekends, resulting in a visible seven-day modulation in the data.

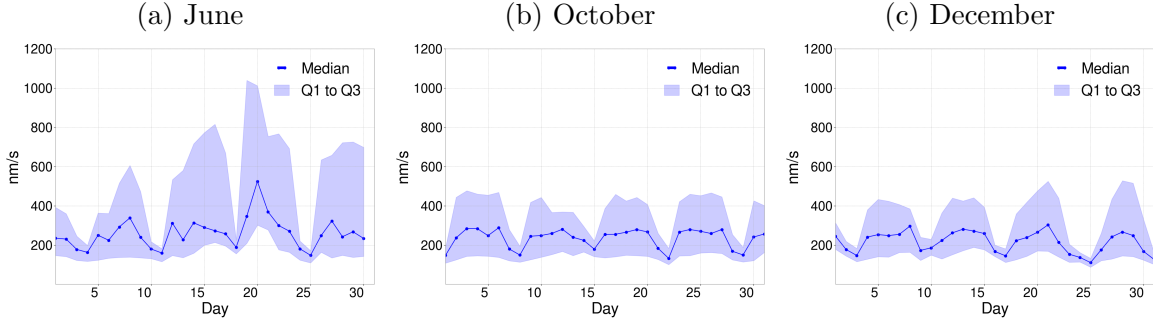


Figure 10: Daily median ground velocity in the anthropogenic band, measured at ETMY in the \hat{z} direction during three months of O4a, where shaded regions indicate the first (Q1) and third (Q3) quartiles. The periodic reduction in noise corresponds to weekends, reflecting lower human activity.

Figure 11 presents the monthly median of the daily ground motion in the \hat{x} direction for the two additional frequency bands defined in this study. The velocity in the LMS band is shown in magenta, while the HMS band is represented in green. In this case, data are plotted exclusively for observing times — that is, the daily median velocity was calculated only during periods when LIGO was operational, to facilitate correspondence with glitch activity. Among all months, May, June, and July exhibited the lowest ground motion, with only slight fluctuations on specific days. July, in particular, had consistently low values throughout the entire month, with the highest number of days exhibiting low ground motion. The t-SNE plots for these same months — Figures 6a, 6b, and 6c — show a predominance of *Group L₂* across all three, with the highest percentage occurring, coincidentally, in July, where *Group L₂* accounts for 53.9% of the data. These results suggest a weak correlation between ground motion and the presence of *Group L₂*.

Beginning in August, ground motion started to increase significantly, reaching higher velocity peaks, particularly in November, December, and January (winter). This trend aligns with the emergence and persistence of the other two clusters (Groups *L₁* and *L₃*) in the t-SNE output. In August, the first month to show a noticeable increase in ground motion on some days, we observe a transition: *Group L₂* is no longer dominant, and its presence continues to decline as ground motion increases.

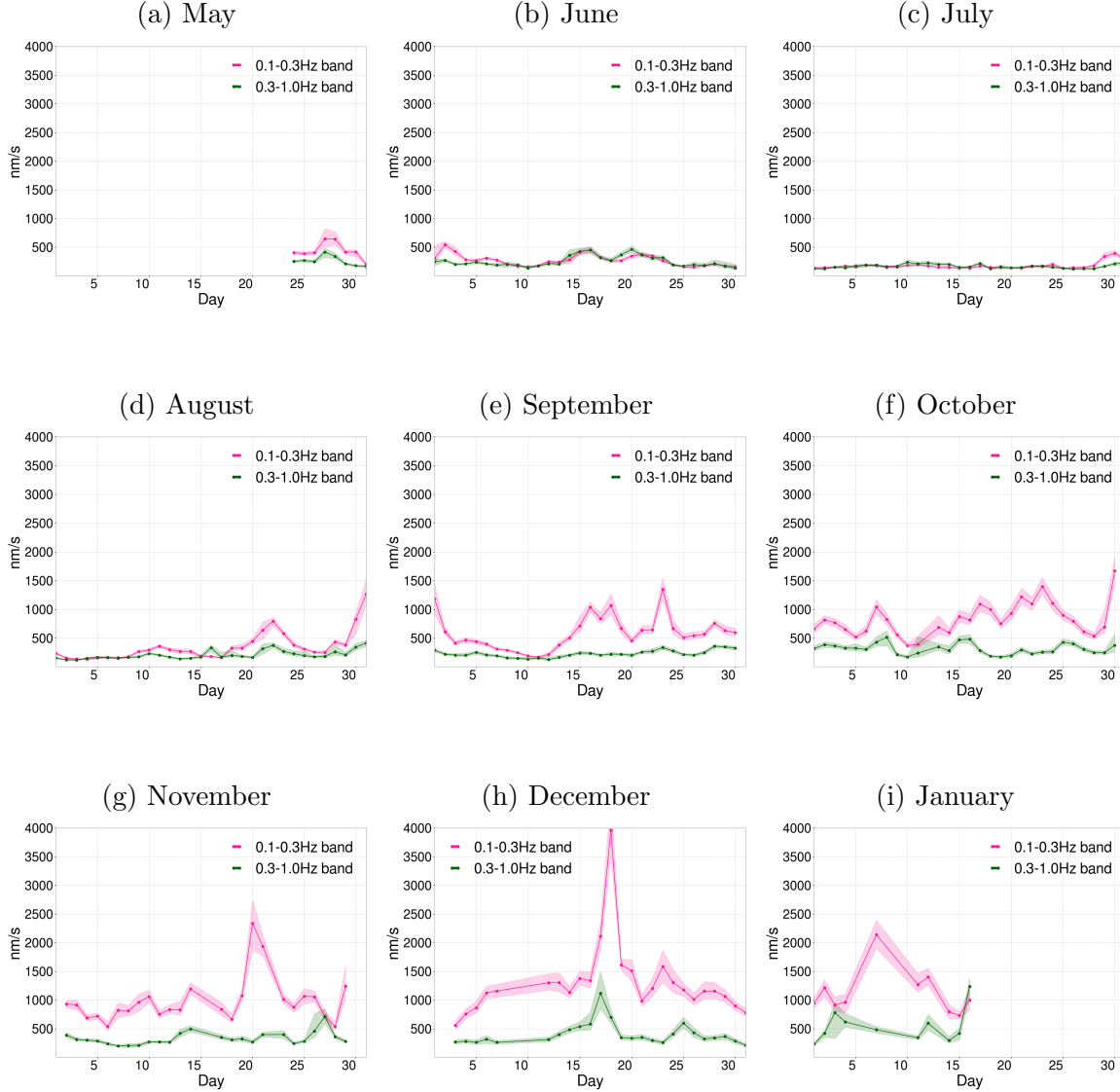


Figure 11: Daily median ground velocity (in the \hat{x} direction) in the lower microseismic band (magenta) and the higher microseismic band (green) for each month during the O4a observing run. The shaded areas represent the first and third quartiles.

This temporal evolution reinforces the weak relationship between Group L₂ and ground motion, while emphasizing the seasonal behavior of Groups L₁ and L₃, which show a strong correlation with increased ground motion.

To further support the main conclusions regarding the relationship between the high rate of low-frequency glitches (associated with Groups L₁ and L₃) and ground motion, we classified all glitches detected at LLO during O4a with frequencies between 10 and 2048 Hz and a minimum SNR of 7.5, assigning each to one of the three previously identified groups. In total, over one hundred thousand glitches were classified. After classifying the glitches, the data were organized to show hourly count of glitches from

each class, across all days. For each corresponding hour, the median ground motion amplitude was also computed for the three defined frequency bands. Figures 12a, 12b, and 12c present the hourly rate of each group as a function of the median ground motion in the LMS, HMS, and anthropogenic bands, respectively.

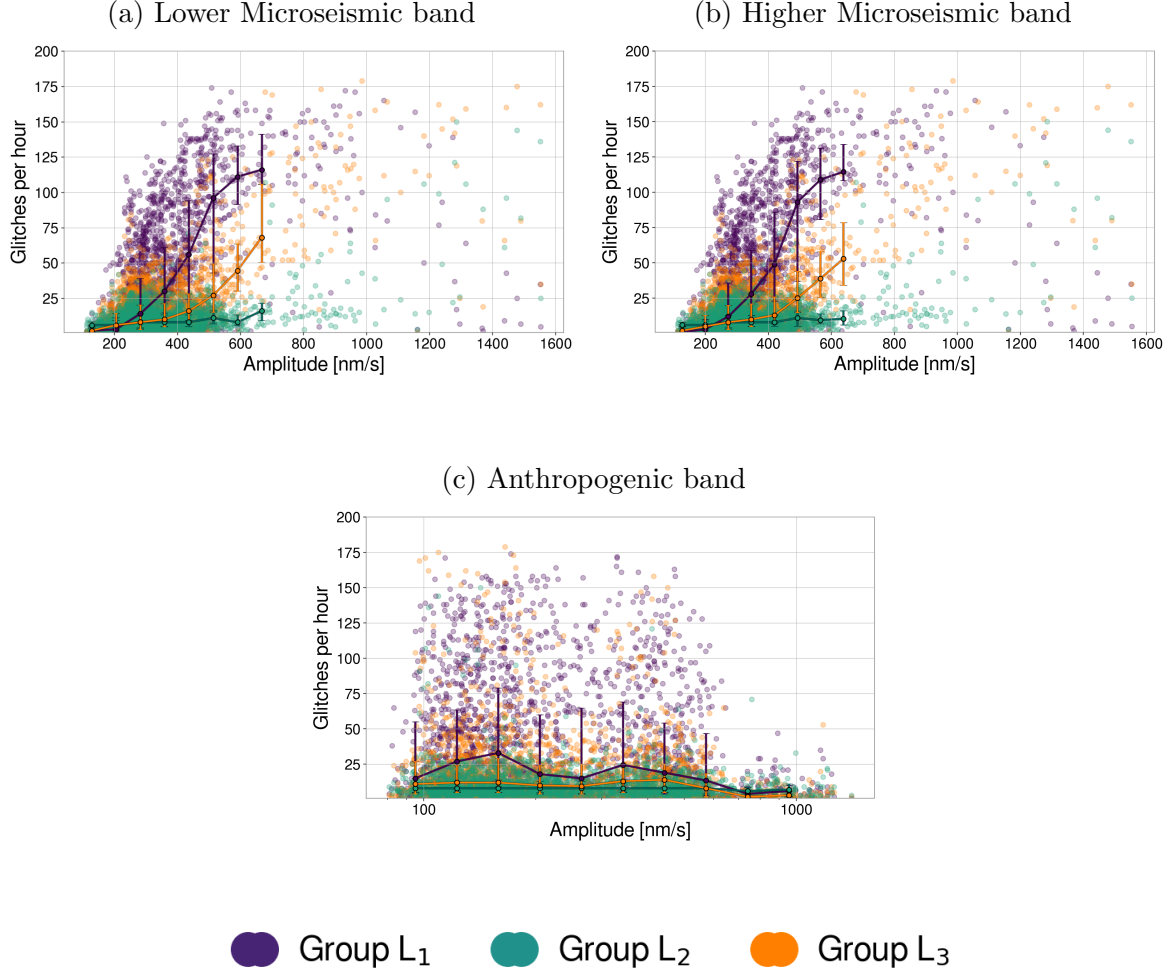


Figure 12: Number of glitches as a function of ground motion amplitude for the three different bands. Each dot represents a measurement interval, color-coded by group. Solid lines indicate the median number of glitches per amplitude bin (computed using the central 98% of the data), with error bars showing the interquartile range.

As shown by the distribution of data points, the glitch rates for Group L₁ (purple) and Group L₃ (orange) exhibit a positive correlation with increasing amplitudes in the LMS and HMS bands (Figures 12a and 12b). In contrast, this trend is not observed for the anthropogenic band, suggesting no significant correlation in that case (Figures 12c). During the O4a period, some anthropogenic activities, such as logging [51,52] took place near the interferometer, leading to unusually high amplitudes in this band (exceeding 600 nm/s); this effect was observed, for example, in June, as illustrated by the variations shown in Figure 10a. Coincidentally, microseismic noise was low at that time, and since

most glitches were associated with microseismic motion, the overall glitch rate remained low. As a result, the region on the right side of Figure 12c behaves as an outlier when compared to the main distribution. This observation reinforces the conclusion that high amplitudes in the anthropogenic band do not significantly affect the glitch rate, confirming that this band did not contribute meaningfully to glitches with $\text{SNR} > 7.5$, as also suggested in [53].

The curves in the figures represent the median glitch rate within amplitude bins, and are shown only when each bin contains at least 20 data points. This criterion helps to exclude sparsely populated bins, minimizing the influence of statistical fluctuations or outliers. Group L_1 appears to exhibit a flatter trend or even a decrease in glitch rate at very high amplitudes of microseismic motion. This effect is attributed to a shift in the peak frequency of the glitches at elevated ground motion levels. Since Group L_1 is typically characterized by a peak frequency around 12 Hz, higher ground motion can shift this peak upward, causing the classifier to instead assign these glitches to Group L_3 , which is defined by a primary peak frequency around 20 Hz. This transition tends to occur when the ground motion amplitude becomes significantly higher.

We quantified the correlation between each identified group and each ground-motion band using the Pearson correlation coefficient (r) [54], which measures the strength of the linear relationship between two variables—in this case, the glitch rate and ground motion in different bands. Table 1 summarizes the correlation coefficients for each case, computed from more than 2,000 valid data points. Overall, the results confirm a strong correlation between Groups L_1 and L_3 and both the LMS and HMS bands, indicating a clear dependence of their occurrence on ground motion; their corresponding p -values (where smaller values mean the correlation is less likely to be due to chance) were below 10^{-100} . Group L_2 exhibits a weak correlation with the LMS band, which may partially arise from classification overlaps or a subclass with such dependence. As expected, none of the groups shows a significant correlation with the anthropogenic band. However, due to high-amplitude outliers associated with anthropogenic activities (previously mentioned), a small negative correlation appears for all three groups, with p -values equal to or below 0.05. Despite these small p -values (likely driven by the large sample size), the corresponding correlation coefficients are very close to zero when considering only ground-motion amplitudes below 600 nm/s (see Table 1), indicating no meaningful linear relationship.

Table 1: Pearson correlation between LMS, HMS, and Anthropogenic bands for Groups L_1 , L_2 , and L_3 .

| Correlation | LMS | HMS | Ant. band |
|-------------|------|------|-----------|
| Group L_1 | 0.64 | 0.63 | -0.03 |
| Group L_2 | 0.32 | 0.17 | -0.04 |
| Group L_3 | 0.53 | 0.47 | -0.05 |

In conclusion, applying t-SNE to unclustered Omicron data from LLO enabled the

identification of two glitch groups that follow the seasonal behavior of microseismic ground motion, providing strong support for the discussion reported in [7].

3. Glitches during O4a at LHO

The rate of glitches with an SNR greater than 10 was significantly lower at LHO during O4a (approximately 6 per hour) compared to O3 (around 17 per hour). However, LHO was notably affected by glitches with lower SNR. When considering glitches with an SNR exceeding 6.5, Hanford experienced an average of 77 glitches per hour during O4a — more than double the glitch rate observed during O3, which was approximately 33 per hour [7]. This increase is attributed to the presence of broadband transient noise between 20–40 Hz during O4a, which occasionally extended to peak frequencies around 50 Hz. The predominance of this frequency range is evident in Figure 13, which shows the histogram of glitches during O4a with an SNR greater than 6.

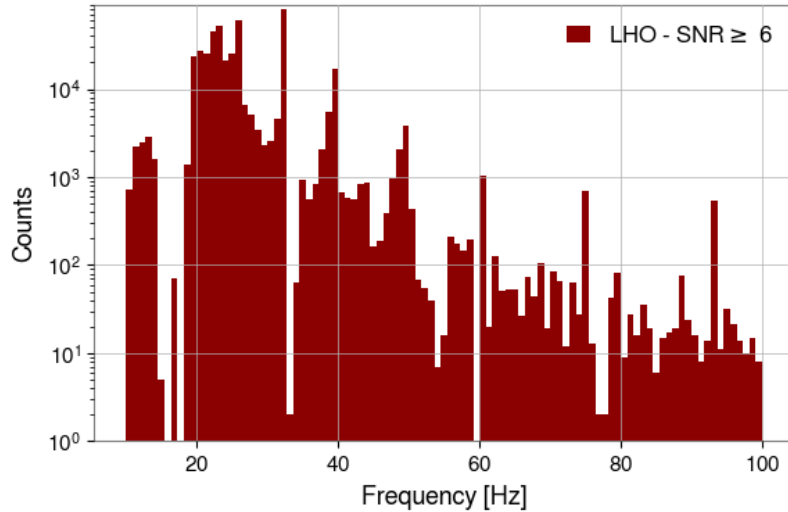


Figure 13: Histogram of glitch frequencies during O4a at LHO. The plot highlights the most common glitch range, between 20 and 40 Hz, considering only glitches with SNR above 6.

In comparison to LLO (Figure 1), LHO exhibits noticeably fewer glitches below 20 Hz, even when lower-SNR glitches are considered. This difference may be attributed to the better low-frequency sensitivity of the Livingston detector. The contrasting sensitivities of the two detectors are illustrated in Figures 14a and 14b, which compare the characteristic strain of LHO (dark red) and LLO (dark blue) on two distinct days during O4a — October 16, 2023, and December 27, 2023 — characterized by relatively low and high levels of microseismic motion, respectively. The dots represent a scatter plot of glitches detected during the same periods, with amplitude plotted against peak frequency. During low microseismic activity (Figure 14a), very few glitches are observed at either observatory, though some broadband glitches remain present at

Hanford. In contrast, during periods of elevated microseismic motion (Figure 14b), both observatories exhibit a higher occurrence of transient noise spanning a broader frequency range, including frequencies below 13 Hz.

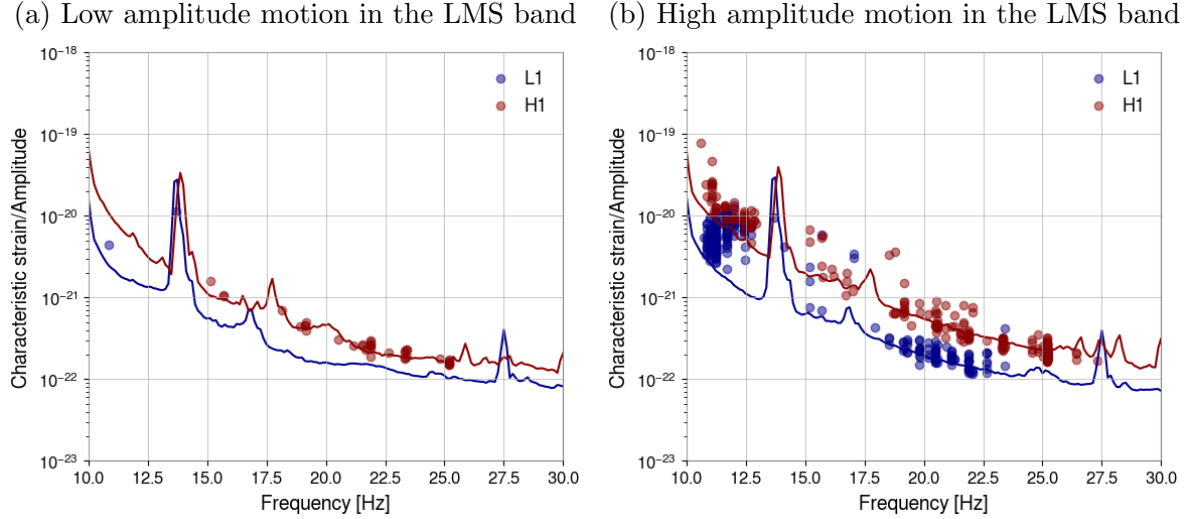


Figure 14: Characteristic strain in Hanford and Livingston over two hours of data during of (a) low and (b) high amplitude motion in the low microseismic (LMS) band—approximately 150 nm/s and 1000 nm/s, respectively. The amplitudes and peak frequencies of the glitches detected during the same periods are shown as dots.

The monthly glitch rate in Hanford data during O4a is shown in Figure 15. The overall trend closely resembles that observed at LLO, with a notable increase beginning in October, but with an additional rise at LHO in July. The broadband glitches in the 20 to 50 Hz range are highlighted by the red bars with diagonal hatching, illustrating their predominance throughout the O4a run, except during May.

By employing the same t-SNE-based methodology, we analyzed the transient glitches observed at LHO during the O4a run. Figure 16a shows the two-dimensional t-SNE projection of the glitches before any classification, while Figure 16b displays the corresponding output after applying the classification procedure. The classified output highlights four main groups, labeled Group H_1 through Group H_4 .

Figure 17 presents the t-SNE scatter plots for LHO, filtered by month, enabling us to track the evolution and persistence of glitch clusters over time. In May, less than one week of data was available, during which Group H_4 dominated the distribution, accounting for more than 80% of the glitches. This group primarily consists of glitches analogous to those observed at LLO — such as *Koi Fish*, *Blip*, and *Extremely Loud* (present in Group L_2) — in addition to low-frequency glitches with a peak frequency around 12 Hz. These low-frequency glitches, which were not as prevalent at LHO as at LLO, occurred over a few hours at the end of May and, due to their low occurrence, they do not form a distinct group at LHO, unlike at LLO. The presence of these glitches

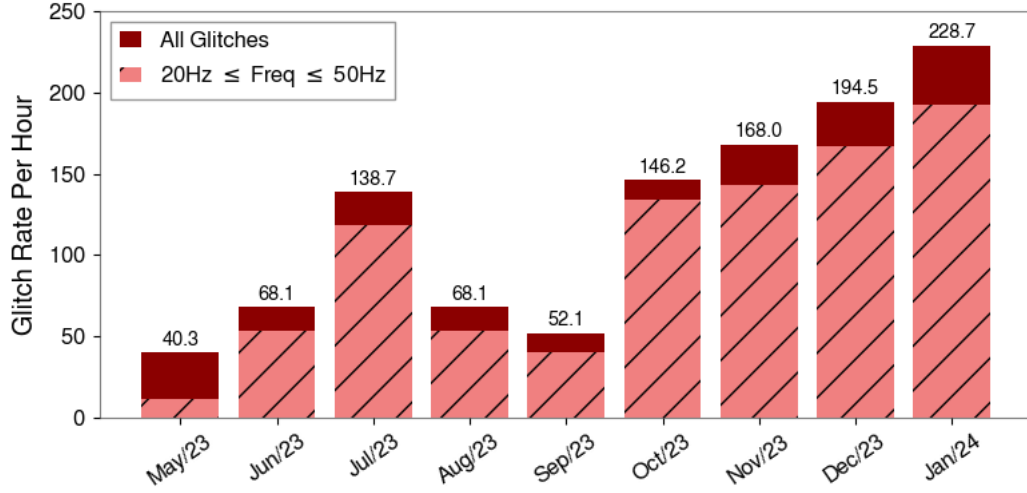


Figure 15: Average glitch rate per hour for each month during O4a at LHO. All clustered Omicron transients between 10 and 2048 Hz with SNR greater than 6 are shown in solid dark red bars, while broadband glitches are indicated by hatched bars.

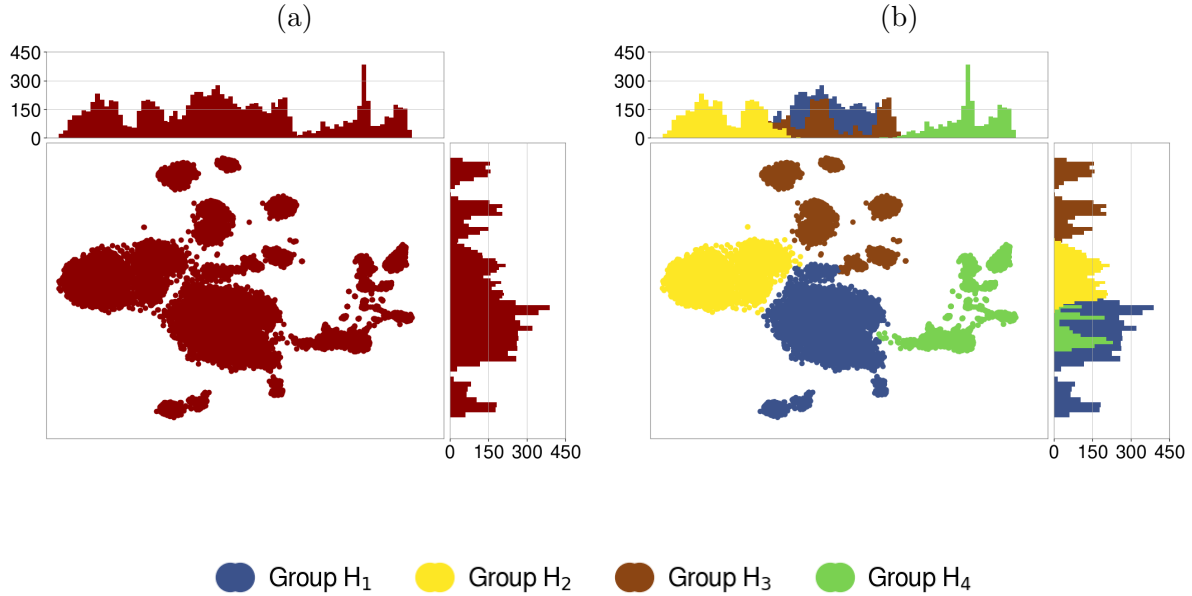


Figure 16: (a) Scatter plot of the 2D t-SNE output coordinates representing 13,500 data points from LHO, each originally in a 1,230-dimensional space, derived from unclustered Omicron triggers. Each point corresponds to a glitch, with clustering based on pairwise similarities. The histograms on the top and right axes illustrate the distribution of glitches along each coordinate. (b) The same t-SNE representation, now with classified data.

in May helps explain the larger discrepancy between the total glitch rate (solid bar) and the rate of broadband glitches (hatched bar) shown in Figure 15.

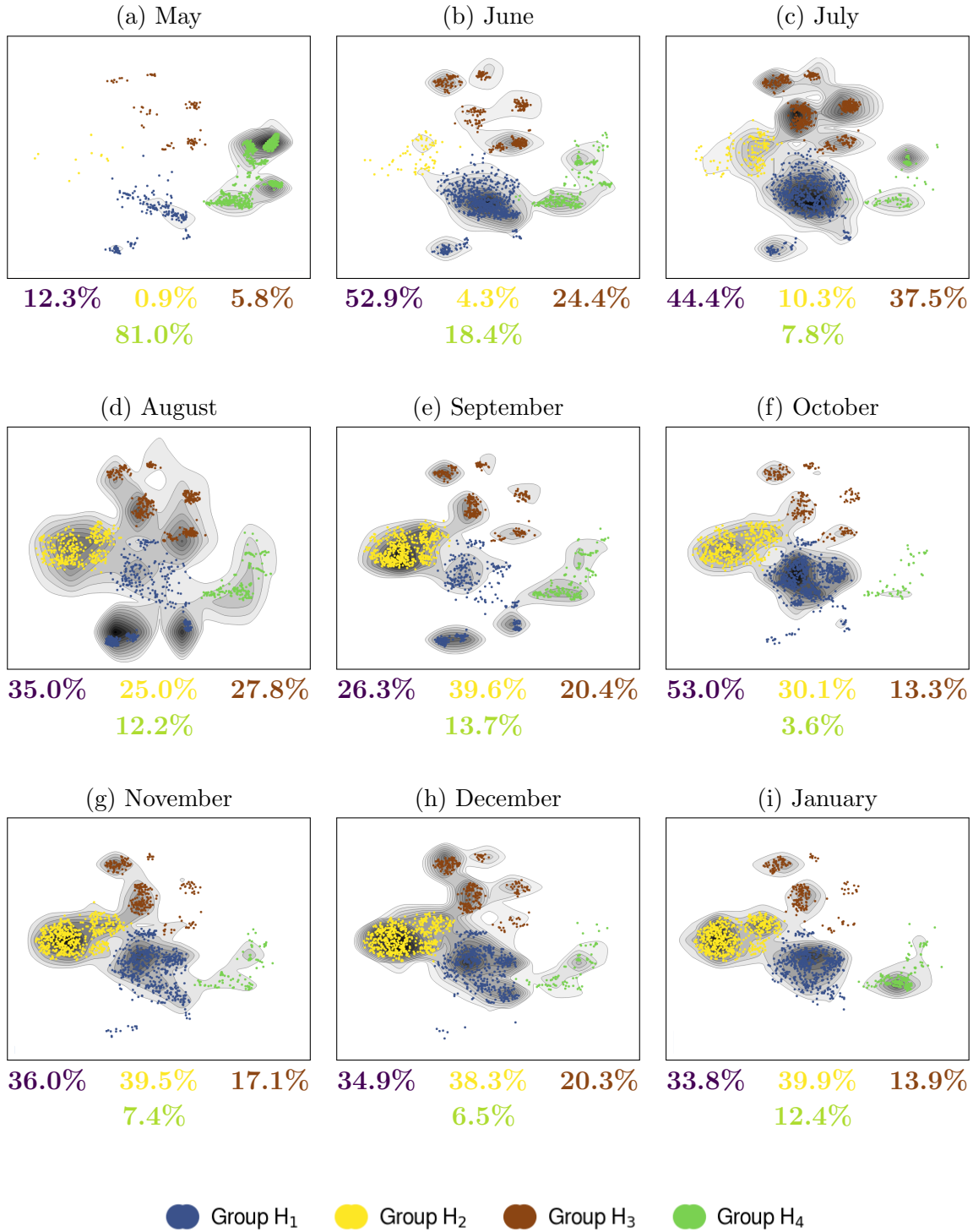


Figure 17: Scatter plots of the same t-SNE coordinates filtered by month (for H₁), showing the evolution of cluster composition from May 2023 to January 2024. Percentages represent the distribution of glitches across the four identified groups.

In June, the bottom-center region of the t-SNE map becomes increasingly prominent, persists through July, and decreases in August and September, coinciding with the activation of other groups and resulting in a more uniform overall distribution. This decrease was driven by the implementation of an improved alignment control system [55], which substantially reduced the occurrence of glitches with SNR greater than 7.5 [56]. This is also reflected in Figure 15, which shows a reduction in the glitch rate from 138.7 to 68.1 glitches per hour between July and August.

From October through January, the large cluster H_1 , together with H_2 , became the most persistent feature in the t-SNE projection, collectively accounting for at least 70% of the observed glitches. Although the implementation of the alignment controller substantially contributed to glitch mitigation, an increase in broadband glitches emerged in October and persisted throughout the remainder of the observing run, leading to the predominance of these two clusters. This increase coincided with the relocation of the LSC (Length Sensing and Control) feedforward path from the ETMX (End Test Mass of the X-arm) to the ETMY actuator [57], which initially reduced noise above 50 Hz but introduced additional noise at lower frequencies. Subsequent investigations suggested that the ETMY R0 ‡ actuator, responsible for length control, may not have been operating properly at that time [59], potentially generating excess scattered light and contributing to the observed rise in glitch rate.

A faulty cable connected to the ETMY R0 actuator was identified as the source of the malfunction [60]; its replacement led to a slight decrease in the glitch rate. This was followed by a new increase, possibly associated with the implementation of an updated feedforward filter in the Signal Recycling Cavity Length (SRCL) control loop of the Length Sensing and Control (LSC) system [61], which was later revised, resulting in a marked decrease in the glitch rate from October 23 onward [62] — this decrease is highlighted by the vertical pink dashed line in Figure 18, where the dark red vertical bars represent the evolution of the hourly glitch rate throughout the entire O4a.

A bicoherence § analysis revealed that these broadband glitches were related to the electrostatic drive (ESD) system in the detector [64]. Positioned behind the test mass, the ESD applied controlled forces to the mirror to maintain the interferometer in its locked state — that is, when all the optical cavities are held on resonance through feedback control — enabling it to operate in observation mode for gravitational-wave detection. The ESD consists of a constant voltage component — commonly referred to as the bias — and multiple lower-voltage components applied at four sections: upper left (UL), upper right (UR), lower left (LL), and lower right (LR). Each of these contributes independently, with voltages that typically vary in amplitude according to the control needs. Together, they enable fine adjustments to the mirror’s position along the length degrees of freedom.

‡ R0 refers to the uppermost stage of the reaction chain [58].

§ Bicoherence [63] is a diagnostic tool that assesses nonlinear coupling between two frequencies. If two frequencies, f_1 and f_2 , are present in a signal, bicoherence can indicate whether a new frequency component at $f_1 + f_2$ (or $f_1 - f_2$) is being generated through nonlinear interactions.

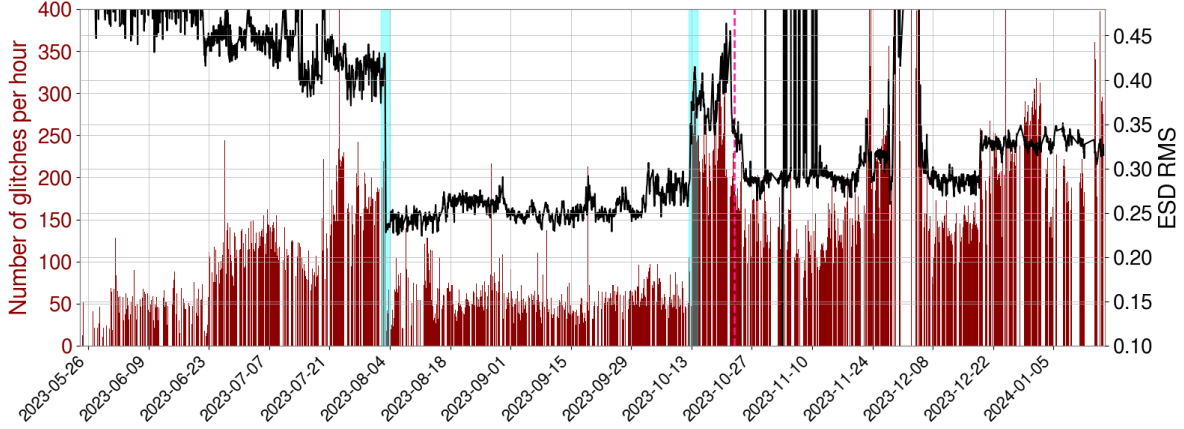


Figure 18: (a) Number of glitches per hour at LHO (dark red) and RMS of the electrostatic drive voltage at the ETMX UL component (black) during O4a. We selected glitches in the 20–50 Hz frequency band and discarded data segments shorter than 20 minutes to avoid peaks caused by a high number of glitches over a short duration. The cyan-shaded bars represent the two main periods when the ESD RMS (and the glitch rate) changed significantly.

Along with the hourly glitch rate during O4a, Figure 18 also presents the RMS value of the ESD voltage for the UL component at ETMX (in black). The impact of the new alignment control system is evident at the beginning of August, with a significant drop in both ESD RMS and glitch rate. Another key moment occurs in October, when both show a substantial increase, related to the reallocation of the LSC feedforward from ETMX to ETMY. The main purpose of this plot is to illustrate that significant changes in the ESD indeed affected the rate of the broadband glitches at LHO during O4a. Although other factors also contributed to transient noise in the detector and influenced the curve behavior [65, 66], a clear correlation can be observed between variations in the ESD RMS signal and fluctuations in the glitch rate, supporting the hypothesis of nonlinear coupling between the ESD actuation system and the detector strain output.

The glitch groups have distinct morphologies, with some becoming more dominant in certain months. The number of classes is determined by their morphological differences, as t-SNE inference primarily relies on the glitch morphology from Omicron. Despite their morphological differences, the analysis of their temporal occurrence suggests that, except for Group H_4 , all the main glitches are likely associated with the same underlying source. Their differences lie primarily in the recurrence and morphology of specific features: vertical “blips” (Figure 19a, predominantly in Group H_1), short-duration horizontal lines (Figure 19b, common in Group H_2), and longer-duration lines that vary in frequency, as well as in the number and timing of repetitions (Figure 19c, more frequent in Group H_3). These variations also explain the presence of smaller subclusters within Group H_3 .

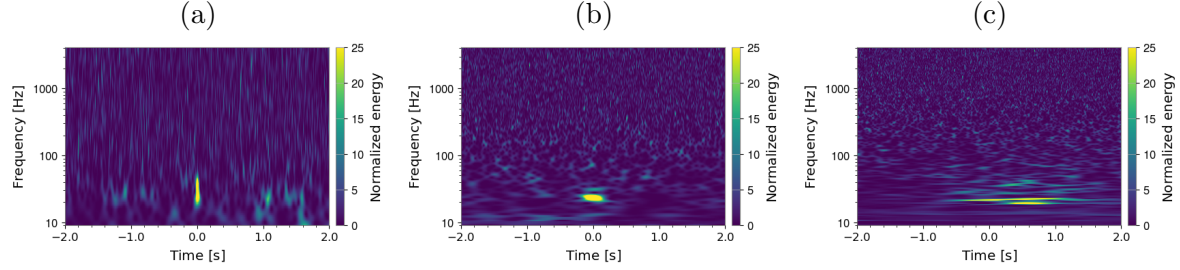


Figure 19: Examples of spectrograms for each of the groups H_1 , H_2 , and H_3 identified at LHO, shown in order.

Glitches observed at Hanford were particularly challenging to characterize, as many were very short in duration and thus better represented using low Q -values, while others required higher Q -values to adequately capture their morphology. The inclusion of a wide range of Q -values allowed for the identification of groups with distinct morphological features, and the monthly distribution of these groups highlights periods when certain classes were more prevalent. The decrease in the number of glitches in Group H_1 during August and September — associated with the implementation of the new controller — contrasts with the increase in Group H_2 during the same period, reinforcing the importance of distinguishing these two groups. As mentioned before, the apparent disappearance of a glitch group does not indicate its absence; it simply reflects a period of reduced prominence.

Figures 20a to 20d show glitch rates during the entire O4a for each group, considering all glitches detected at LHO with a minimum SNR of 6, which were classified according to the four identified groups. Only Group H_4 deviates from the overall trend of broadband glitches shown in Figure 18, as expected given its morphological composition. The y-axis scales differ across panels, highlighting the predominance of Group H_1 , followed by Group H_2 , consistent with the monthly t-SNE behavior.

To support the hypothesis of no correlation between the ESD and Group H_4 , Figure 21b shows a scatter plot of the hourly glitch rate for all O4a data classified as Group H_4 versus the median ESD over the same periods, revealing no apparent correlation. The curve representing the median glitch rate is shown only for bins containing at least 20 data points. In contrast, the same type of plot for all glitches classified as H_1 — the most predominant broadband group — illustrates a clear linear correlation in Figure 21a, highlighting the distinct behavior of these two groups.

The correlation between the glitch rate and ESD RMS for these two groups was also quantitatively estimated using the Pearson correlation coefficient (r) [54]. The analysis confirmed a lack of correlation for Group H_4 ($r = 0.12$) and a strong positive correlation for Group H_1 with $r = 0.76$. For these plots and numbers, we focus on data collected after October, when the ESD exhibited significant oscillations. Between August and October, the correlation was not evident, as the ESD remained nearly constant (see

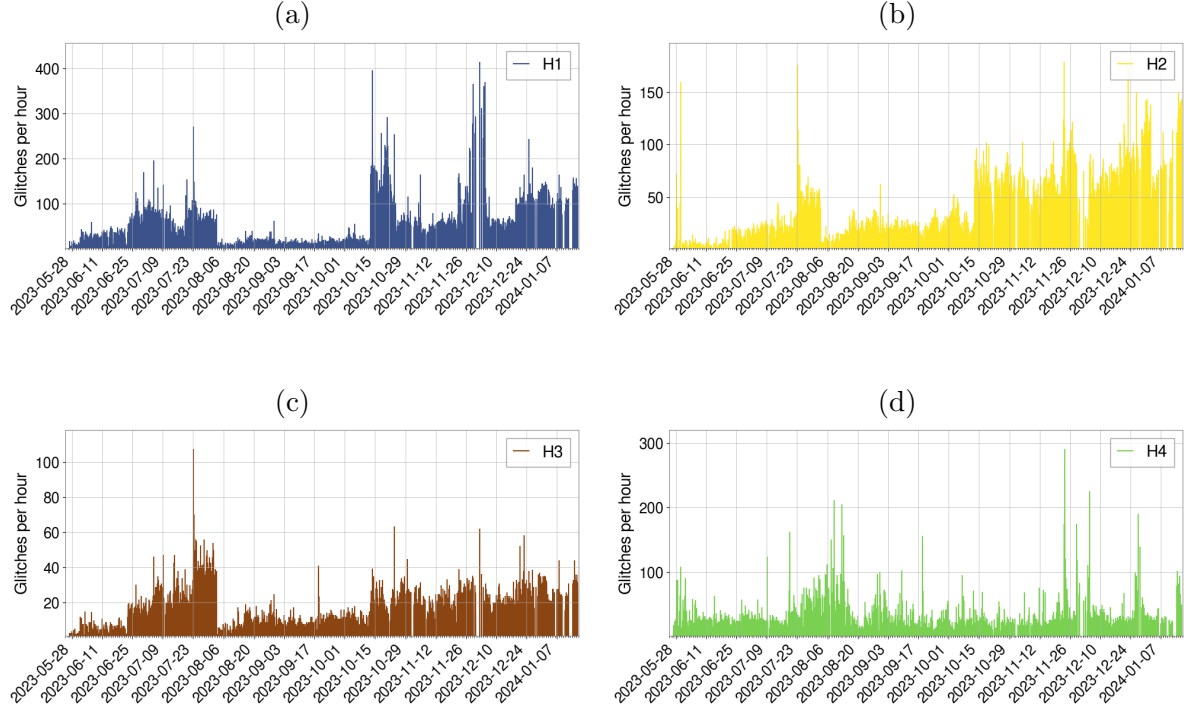


Figure 20: Number of glitches per hour observed in each hour of O4a at LHO for all glitches classified into the identified classes. For this plot, we discarded data segments shorter than 20 minutes to avoid peaks caused by a high number of glitches over a short duration.

Figure 18). Likewise, the same plot using data prior to August does not show this correlation, which remains not fully understood, given that broadband glitches appear to originate from the same key source.

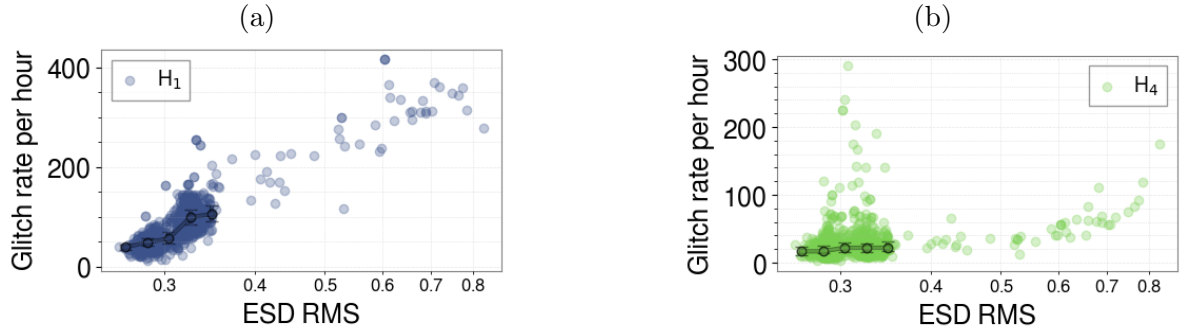


Figure 21: Hourly glitch rate for all O4a glitches at LHO classified as (a) Group H_1 and (b) Group H_4 . For these plots, data segments shorter than 20 minutes were discarded.

Although these glitches affected the entire O4a, dedicated testing and efforts by the

LHO team led to the implementation of a new feedback control configuration, which significantly reduced the noise and resulted in a more stable and stationary system by lowering the ESD drive voltage. This improved configuration was adopted for the O4b observing run, which began with no recurrence of these glitches [67–70].

4. Conclusions and Discussions

This paper presents an analysis of the main glitch groups observed during O4a at the LIGO observatories. We employed a fully unsupervised machine learning framework, based on t-distributed Stochastic Neighbor Embedding (t-SNE) followed by Agglomerative Clustering, to investigate their behavior. This approach reduces the high-dimensional representation of glitches, built from unclustered Omicron data across all Q-values, into a two-dimensional space where morphological similarities emerge. By applying this methodology independently to data from LLO and LHO, we were able to identify dominant glitch populations, track their evolution over time, and correlate their occurrence with environmental or instrumental conditions.

At Livingston, the most prominent glitch populations during O4a were closely correlated with seasonal variations in ground motion, particularly within the 0.1–1 Hz frequency range. The applied methodology identified three main groups. Two of them — characterized by arch-like spectrogram morphologies, with peak frequencies around 12 Hz and 20 Hz, respectively — were dominant during months of elevated ground motion, which began to increase in the autumn and peaked during the winter in the United States. These two groups exhibited a strong positive correlation with ground velocity in both the lower (0.1–0.3 Hz) and higher (0.3–1 Hz) microseismic bands, but not in the anthropogenic band (1–3 Hz). By contrast, the third group, composed primarily of known classes such as *Blip*, *Tomte*, and *Koi Fish*, stood out during periods of low ground motion and showed no significant dependence on any of the seismic frequency bands tested.

At Hanford, a different glitch landscape was observed. The detector experienced a high occurrence of broadband glitches in the 20–50 Hz range, particularly at lower SNR. These glitches, persistent throughout O4a, were shown to be associated with the electrostatic drive (ESD) system, as indicated by their correlation with the RMS of the applied ESD voltage. In total, four groups were identified using our methodology: three were related to the ESD, and one was not — the latter consisting mainly of known glitch classes such as *Extremely Loud*, *Blip*, and *Low Frequency Lines*. While the three ESD-related groups appeared to share a common instrumental origin, they exhibited distinct morphologies. We also found evidence that some detector tests affected only one of the glitch groups while leaving the others unchanged. This observation highlights the importance of analyzing the groups separately — an analysis made possible by the methodology applied in this work.

The technique aims to uncover the monthly behavior of glitches in gravitational-wave detectors such as LIGO, Virgo, and KAGRA. The only requirement is access to

Omicron data — or a similar tool capable of identifying triggers that encode glitch morphology. Once the glitches are tracked, the ideal next step — as demonstrated in this study — is to examine relevant detector logbook entries that document changes or interventions at the observatories, in order to correlate the behavior of glitch groups with those modifications. By analyzing monthly trends during O4a, we were able to correlate certain glitch groups with environmental or instrumental conditions, providing strong indications of their possible origin. As discussed in the methods paper [35], this approach can be applied at different timescales depending on the specific goals. Although the methodology autonomously identifies glitch groups, human interpretation — along with association to auxiliary channels and documented changes in the observatories — remains essential to understanding their physical origin.

Acknowledgments

We would like to thank Elenna Capote and Jess McIver, for their very useful insights, comments, and suggestions. We express our gratitude to the members of the LIGO Detector Characterization Group and the LIGO-Virgo-KAGRA (LVK) collaboration for their valuable discussions. This work was supported by the National Science Foundation under grant numbers PHY-2110509 and PHY-2409740. The material is based upon work supported by NSF’s LIGO Laboratory, a major facility fully funded by the National Science Foundation. Additionally, the work utilizes the LIGO computing clusters and data from the Advanced LIGO detectors; the authors are grateful for the computational resources provided by the LIGO Laboratory, supported by National Science Foundation Grants PHY-0757058 and PHY-0823459.

Appendix A. Ground motion measurements

This appendix presents a comparison of measurements from seismometers located near the test masses at the LIGO Livingston observatory. Two months were selected for this analysis: July, which exhibits relatively low microseismic motion, and December, which shows high ground motion. The seismometer channels follow the naming convention shown in Table A1, where each channel name consists of the component identifier (e.g., ETM), representing the selected test mass, followed by the corresponding arm, and the motion direction: \hat{x} for motion along the laser direction, \hat{y} for motion perpendicular to the laser, and \hat{z} for vertical motion, perpendicular to the x - y plane.

Figures A1, A2, and A3 show a comparison of ground motion in the three spatial directions for ITMX, ETMX, and ETMY, respectively. For each seismometer, the root mean square (RMS) velocity data are presented across three frequency bands: LMS (lower microseismic band, 0.1–0.3Hz), HMS (higher microseismic band, 0.3–1.0Hz), and anthropogenic band (1.0–3.0 Hz). Each data point represents the daily median velocity measured by the seismometer, and the shaded regions indicate the first and third quartiles.

Table A1: Seismometer channels and corresponding position, arm, and motion directions.

| Channel Name | Position | Arm | Motion Direction |
|--------------|-----------------|-----|-----------------------------------|
| ITMX_X/Y/Z | Input Test Mass | X | \hat{x} / \hat{y} / \hat{z} |
| ITMY_X/Y/Z | Input Test Mass | Y | \hat{x} / \hat{y} / \hat{z} |
| ETMX_X/Y/Z | End Test Mass | X | \hat{x} / \hat{y} / \hat{z} |
| ETMY_X/Y/Z | End Test Mass | Y | \hat{x} / \hat{y} / \hat{z} |

By evaluating all days in both months, we observe that, in general, the motion in the three directions follows similar trends, suggesting that any directional component can be informative when analyzing behavioral variations. In terms of amplitude, for the LMS and HMS bands, motion in the \hat{x} and \hat{y} directions is similar and generally larger than in the \hat{z} direction. Conversely, in the anthropogenic band, the \hat{z} direction exhibits higher amplitudes and larger variations.

We also present comparisons between seismometers located at different positions. After observing that the \hat{x} and \hat{y} directions show very similar behavior in both the LMS and HMS bands, we selected \hat{x} as representative for these two, and \hat{z} for the anthropogenic band. Only one month (June) is presented, as both months lead to the same conclusions. Figure A4 shows a comparison between ITMX and ITMY using the same daily median data. As expected, the signals are nearly identical due to the proximity of the sensors. Figure A5 compares ETMX and ETMY, which exhibit very similar median amplitudes and variations for the LMS and HMS bands. In the anthropogenic band, however, ETMY shows higher median values and larger variations than ETMX, likely due to its closer proximity to nearby roads.

ITMX: Comparison of motion directions

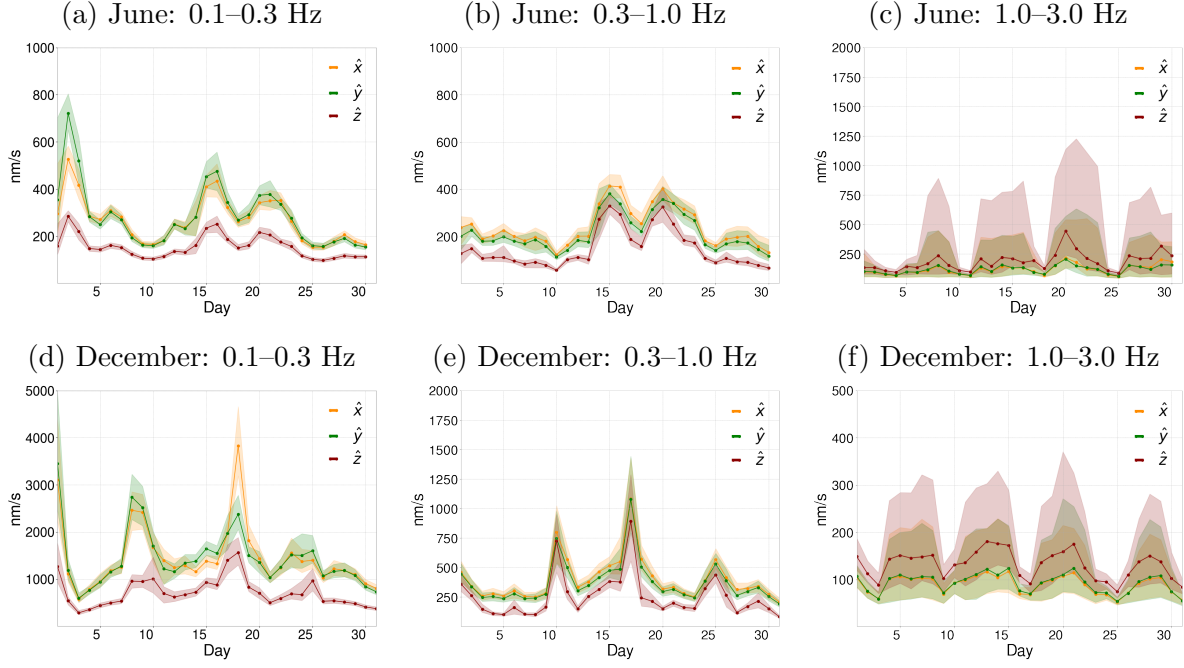


Figure A1: Comparison of motion directions at ITMX during June and December across three frequency bands.

ETMX: Comparison of motion directions

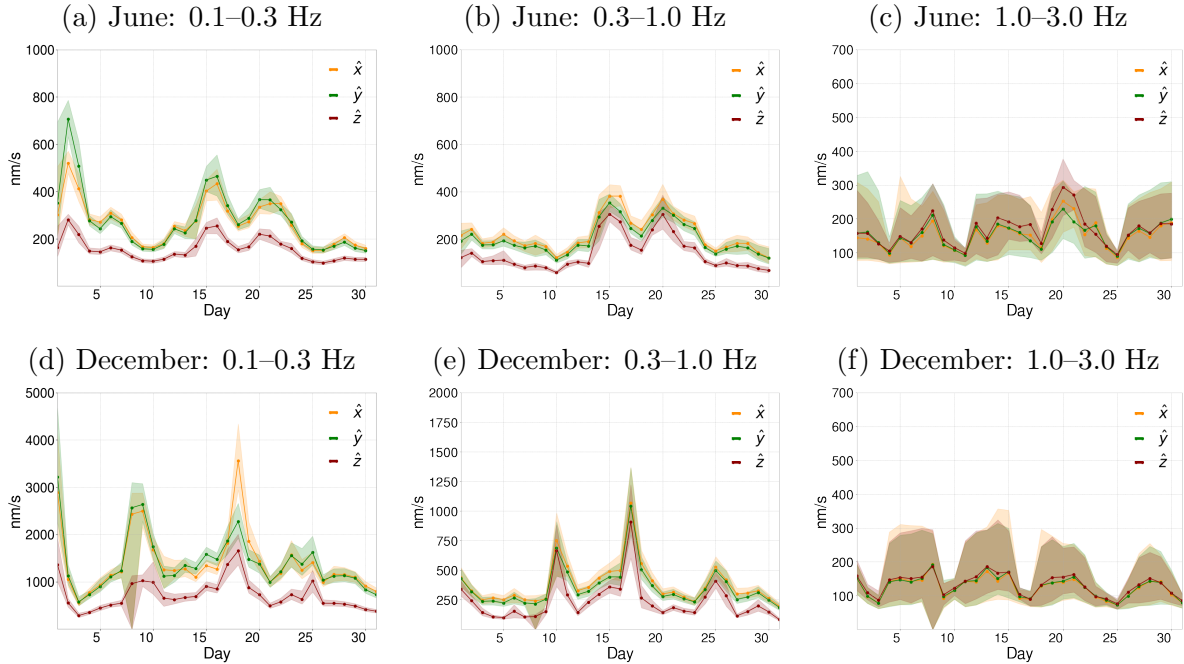


Figure A2: Comparison of motion directions at ETMX during June and December across three frequency bands

ETMY: Comparison of motion directions

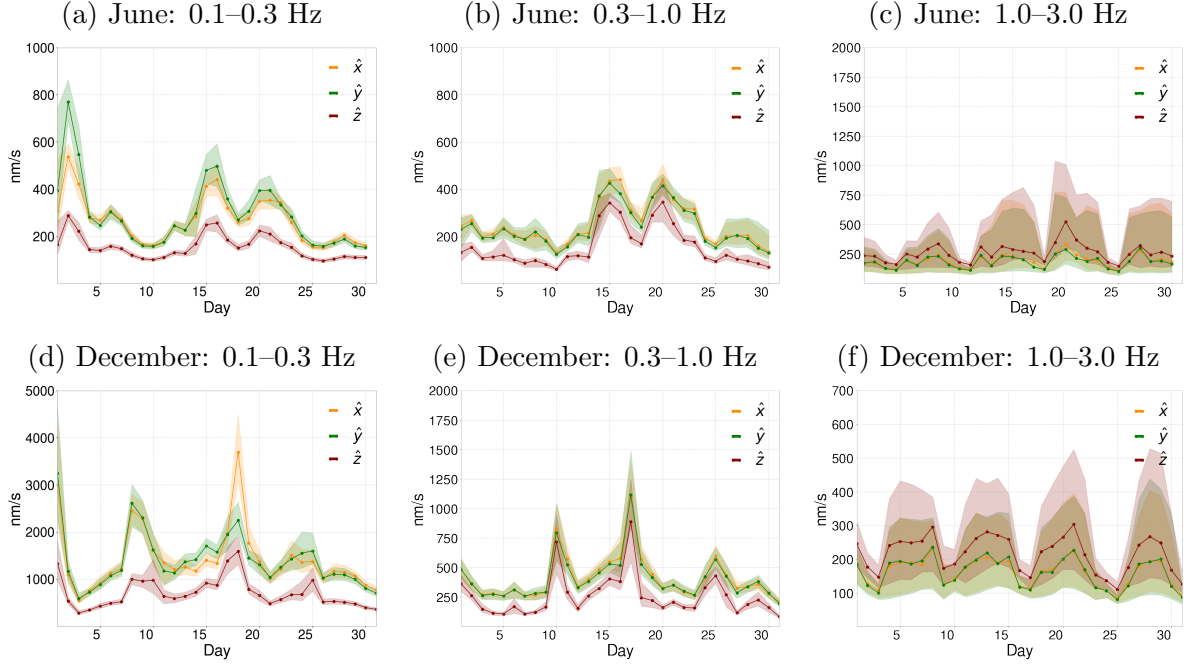


Figure A3: Comparison of motion directions at ETMY during June and December across three frequency bands

ITMX vs. ITMY

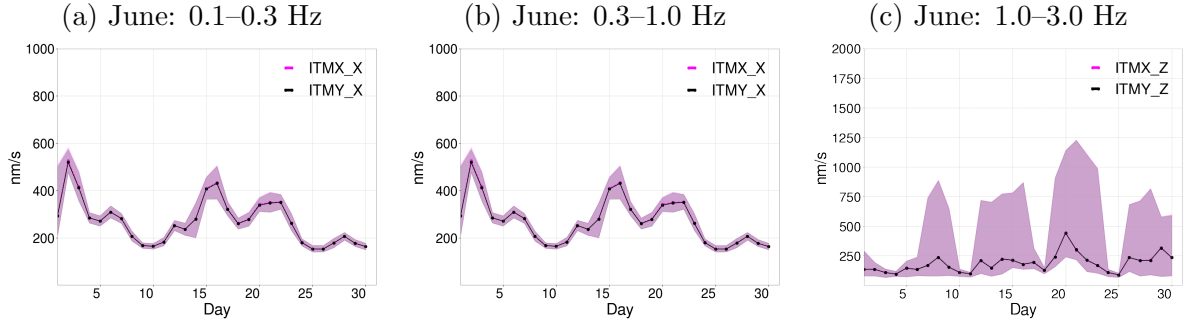


Figure A4: Comparison between ITMX and ITMY during June.

ETMX vs. ETMY

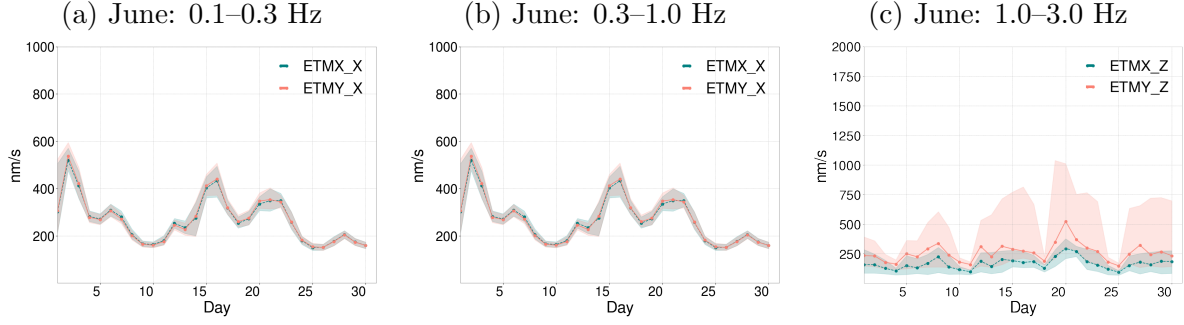


Figure A5: Comparison between ETMX and ETMY during June.

References

- [1] Aasi J *et al.* (LIGO Scientific) 2015 *Class. Quant. Grav.* **32** 074001 (*Preprint* [1411.4547](#))
- [2] Acernese F *et al.* (VIRGO) 2015 *Class. Quant. Grav.* **32** 024001 (*Preprint* [1408.3978](#))
- [3] Akutsu T, Ando M, Arai K, Arai Y, Araki S, Araya A, Aritomi N, Aso Y, Bae S, Bae Y *et al.* 2021 *Progress of Theoretical and Experimental Physics* **2021** 05A101
- [4] Capote E, Jia W, Aritomi N, Nakano M, Xu V, Abbott R, Abouelfettouh I, Adhikari R, Ananyeva A, Appert S *et al.* 2025 *Physical Review D* **111** 062002
- [5] LVK Ligo/virgo/kagra public alerts <https://gracedb.ligo.org/superevents/public/04/>
- [6] Davis D, Areeda J S, Berger B K, Bruntz R, Effler A, Essick R, Fisher R, Godwin P, Goetz E, Helmling-Cornell A *et al.* 2021 *Classical and Quantum Gravity* **38** 135014
- [7] Soni S, Berger B, Davis D, Di Renzo F, Effler A, Ferreira T, Glanzer J, Goetz E, González G, Helmling-Cornell A *et al.* 2025 *Classical and Quantum Gravity* **42** 085016
- [8] Glanzer J, Banagiri S, Coughlin S, Soni S, Zevin M, Berry C P L, Patane O, Bahaadini S, Rohani N, Crowston K *et al.* 2023 *Classical and Quantum Gravity* **40** 065004
- [9] Guimaraes A 2023 *Bridging the Gap Between Detector Characterization and Gravitational Wave Searches in LIGO* Ph.D. thesis Louisiana State University and Agricultural & Mechanical College
- [10] Yarbrough Z, Guimaraes A, Joshi P, Gonzalez G and Valentini A F 2025 *Classical and Quantum Gravity*
- [11] Usman S A, Nitz A H, Harry I W, Biwer C M, Brown D A, Cabero M, Capano C D, Dal Canton T, Dent T, Fairhurst S *et al.* 2016 *Classical and Quantum Gravity* **33** 215004
- [12] Dal Canton T, Nitz A H, Gadre B, Davies G S C, Villa-Ortega V, Dent T, Harry I and Xiao L 2021 *The Astrophysical Journal* **923** 254
- [13] Messick C, Blackburn K, Brady P, Brockill P, Cannon K, Cariou R, Caudill S, Chamberlin S J, Creighton J D, Everett R *et al.* 2017 *Physical Review D* **95** 042001
- [14] Sachdev S, Caudill S, Fong H, Lo R K, Messick C, Mukherjee D, Magee R, Tsukada L, Blackburn K, Brady P *et al.* 2019 *arXiv preprint arXiv:1901.08580*
- [15] Adams T, Buskulic D, Germain V, Guidi G, Marion F, Montani M, Mours B, Piergiovanni F and Wang G 2016 *Classical and Quantum Gravity* **33** 175012
- [16] Aubin F, Brighenti F, Chierici R, Estevez D, Greco G, Guidi G M, Juste V, Marion F, Mours B, Nitoglia E *et al.* 2021 *Classical and Quantum Gravity* **38** 095004
- [17] Hooper S, Chung S K, Luan J, Blair D, Chen Y and Wen L 2012 *Physical Review D—Particles, Fields, Gravitation, and Cosmology* **86** 024012
- [18] Chu Q 2017
- [19] Chu Q, Kovalam M, Wen L, Slaven-Blair T, Bosveld J, Chen Y, Clearwater P, Codoreanu A, Du

- Z, Guo X *et al.* 2022 *Physical Review D* **105** 024023
- [20] Chatterji S, Blackburn L, Martin G and Katsavounidis E 2004 *Classical and Quantum Gravity* **21** S1809
 - [21] Cornish N J and Littenberg T B 2015 *Classical and Quantum Gravity* **32** 135012
 - [22] Cornish N J, Littenberg T B, Bécsy B, Chatziioannou K, Clark J A, Ghonge S and Millhouse M 2021 *Physical Review D* **103** 044006
 - [23] Chatterjee C and Jani K 2025 *The Astrophysical Journal* **982** 102
 - [24] Lopez M, Boudart V, Schmidt S and Caudill S 2022 *arXiv preprint arXiv:2205.09204*
 - [25] Lopez M, Schmidt S and di Renzo D F 2025 *Gravitational Wave Science with Machine Learning* 25
 - [26] George D, Shen H and Huerta E A 2018 *Phys. Rev. D* **97**(10) 101501 URL <https://link.aps.org/doi/10.1103/PhysRevD.97.101501>
 - [27] Powell J, Torres-Forné A, Lynch R, Trifirò D, Cuoco E, Cavaglià M, Heng I S and Font J A 2017 *Classical and Quantum Gravity* **34** 034002
 - [28] Chan M L, McIver J, Mahabal A, Messick C, Haggard D, Raza N, Lecoeuche Y, Sutton P J, Ewing B, Di Renzo F *et al.* 2024 *The Astrophysical Journal* **972** 50
 - [29] Razzano M, Di Renzo F, Fidecaro F, Hemming G and Katsanevas S 2023 *Nuclear Instruments and Methods in Physics Research Section A: Accelerators, Spectrometers, Detectors and Associated Equipment* **1048** 167959
 - [30] Alvarez-Lopez S, Liyanage A, Ding J, Ng R and McIver J 2024 *Classical and Quantum Gravity* **41** 085007
 - [31] Zevin M, Jackson C B, Doctor Z, Wu Y, Østerlund C, Johnson L C, Berry C P, Crowston K, Coughlin S B, Kalogera V *et al.* 2024 *The European Physical Journal Plus* **139** 100
 - [32] Zevin M, Coughlin S, Bahaadini S, Besler E, Rohani N, Allen S, Cabero M, Crowston K, Katsaggelos A K, Larson S L *et al.* 2017 *Classical and quantum gravity* **34** 064003
 - [33] Zooniverse / Gravity Spy Project and Gravity spy <https://www.zooniverse.org/projects/zooniverse/gravity-spy> accessed: 2025-06-05
 - [34] Cabero M, Lundgren A, Nitz A H, Dent T, Barker D, Goetz E, Kissel J S, Nuttall L K, Schale P, Schofield R *et al.* 2019 *Classical and Quantum Gravity* **36** 155010
 - [35] Ferreira T A and González G 2024 *Classical and Quantum Gravity*
 - [36] Robinet F 2016 Omicron: an algorithm to detect and characterize transient events in gravitational-wave detectors
 - [37] Robinet F, Arnaud N, Leroy N, Lundgren A, Macleod D and McIver J 2020 *SoftwareX* **12** 100620
 - [38] Brown J C 1991 *The Journal of the Acoustical Society of America* **89** 425–434
 - [39] Van der Maaten L and Hinton G 2008 *Journal of machine learning research* **9**
 - [40] Ferreira T A and Costa C A 2022 *Classical and Quantum Gravity* **39** 165013
 - [41] Xu R and Wunsch D 2005 *IEEE Transactions on neural networks* **16** 645–678
 - [42] Rousseeuw P J 1987 *Journal of computational and applied mathematics* **20** 53–65
 - [43] Soni S, Austin C, Effler A, Schofield R, González G, Frolov V, Driggers J C, Pele A, Urban A, Valdes G *et al.* 2020 *Classical and Quantum Gravity* **38** 025016
 - [44] Soni S, Glanzer J, Effler A, Frolov V, González G, Pele A and Schofield R 2024 *Classical and Quantum Gravity* **41** 135015
 - [45] Accadia T, Acernese F, Antonucci F, Astone P, Ballardin G, Barone F, Barsuglia M, Bauer T S, Beker M, Belletoile A *et al.* 2010 *Classical and Quantum Gravity* **27** 194011
 - [46] Ferreira T A and González G *Low Frequency Burst or Scattered Light?* <https://alog.ligo-la.caltech.edu/aLOG/index.php?callRep=68208>
 - [47] Daw E, Giaime J, Lormand D, Lubinski M and Zweizig J 2004 *Classical and Quantum Gravity* **21** 2255
 - [48] Pedregosa F, Varoquaux G, Gramfort A, Michel V, Thirion B, Grisel O, Blondel M, Prettenhofer P, Weiss R, Dubourg V *et al.* 2011 *the Journal of machine Learning research* **12** 2825–2830
 - [49] Waskom M L 2021 *Journal of Open Source Software* **6** 3021

- [50] Wu Y, Zevin M, Berry C P, Crowston K, Østerlund C, Doctor Z, Banagiri S, Jackson C B, Kalogera V and Katsagelos A K 2025 *Classical and Quantum Gravity* **42** 165015
- [51] Fyffe M *Night Operators Log* <https://alog.ligo-la.caltech.edu/aLOG/index.php?callRep=65597>
- [52] arnaud P *Lockloss @ 16:34 UTC* <https://alog.ligo-la.caltech.edu/aLOG/index.php?callRep=65627>
- [53] Gonzalez G *et al.* There is no significant change in the trend of glitches throughout the day with and without logging present LIGO aLOG 77176. Available at: <https://alog.ligo-la.caltech.edu/aLOG/index.php?callRep=77176>
- [54] Benesty J, Chen J, Huang Y and Cohen I 2009 Pearson correlation coefficient *Noise reduction in speech processing* (Springer) pp 1–4
- [55] Vajente G *Low frequency noise improved with new CHARD Y controller and reduced TM damping* <https://alog.ligo-wa.caltech.edu/aLOG/index.php?callRep=71927>
- [56] Glanzer J *Low frequency noise improved with new chard_y controller and reduced tm damping* LIGO aLOG 71933. Available at: <https://alog.ligo-wa.caltech.edu/aLOG/index.php?callRep=71933>
- [57] Driggers J and Compton C *LSC FF moved from ETMX to ETMY PUM* <https://alog.ligo-wa.caltech.edu/aLOG/index.php?callRep=73420>
- [58] Colgan R E, Marka Z, Yan J, Bartos I, Wright J N and Marka S 2023 *Physical Review D* **107** 062006
- [59] Driggers J *et al.* *ETMY R0 may be not actuating, so EY R0 tracking may not be working* <https://alog.ligo-wa.caltech.edu/aLOG/index.php?callRep=73447>
- [60] Fil, Dave and Rahul *ETMY R0 Binary Test Coil I/O (F1 and F2 channels) up and working again - caused due to faulty cable.* <https://alog.ligo-wa.caltech.edu/aLOG/index.php?callRep=73522>
- [61] Compton C *LSC Feedforward and Low frequency DARM noise.* <https://alog.ligo-wa.caltech.edu/aLOG/index.php?callRep=73561>
- [62] Vajente G *New SRCLFF improved DARM RMS a bit and improved 20-50 Hz noise a bit too.* <https://alog.ligo-wa.caltech.edu/aLOG/index.php?callRep=73662>
- [63] Choudhury S M, Shah S L, Thornhill N F, Choudhury S M, Shah S L and Thornhill N F 2008 *Diagnosis of Process Nonlinearities and Valve Stiction: Data Driven Approaches* 29–41
- [64] Basalaev A *et al.* *Projection of ESD quadratic noise* <https://alog.ligo-wa.caltech.edu/aLOG/index.php?callRep=71005>
- [65] Shaffer T *et al.* *Slightly higher than normal 3-10Hz ground motion today* <https://alog.ligo-wa.caltech.edu/aLOG/index.php?callRep=73550>
- [66] Vajente G *Improving DARM RMS with resonant gains.* <https://alog.ligo-wa.caltech.edu/aLOG/index.php?callRep=73740>
- [67] Compton C and Dartez L *Tuesday morning testing: new darm loop configuration, simulates test, michff* <https://alog.ligo-wa.caltech.edu/aLOG/index.php?callRep=74887>
- [68] Dartez L, Dwyer S and Vajente G *New DARM offloading reduces non-stationarity by reducing ESD drive RMS.* <https://alog.ligo-wa.caltech.edu/aLOG/index.php?callRep=74939>
- [69] Capote E *Another appraisal of pre-O4b sensitivity.* <https://alog.ligo-wa.caltech.edu/aLOG/index.php?callRep=76449>
- [70] Vajente G *New DARM offloading improves low frequency noise level and stationarity.* <https://alog.ligo-wa.caltech.edu/aLOG/index.php?callRep=76459>